

Deep learning-based automated underground cavity detection using three-dimensional ground penetrating radar

Structural Health Monitoring

1–13

© The Author(s) 2019

Article reuse guidelines:

sagepub.com/journals-permissions

DOI: 10.1177/1475921719838081

journals.sagepub.com/home/shm



Man-Sung Kang¹, Namgyu Kim², Jong Jae Lee²  and Yun-Kyu An¹ 

Abstract

Three-dimensional ground penetrating radar data are often ambiguous and complex to interpret when attempting to detect only underground cavities because ground penetrating radar reflections from various underground objects can appear like those from cavities. In this study, we tackle the issue of ambiguity by proposing a system based on deep convolutional neural networks, which is capable of autonomous underground cavity detection beneath urban roads using three-dimensional ground penetrating radar data. First, a basis pursuit-based background filtering algorithm is developed to enhance the visibility of underground objects. The deep convolutional neural network is then established and applied to automatically classify underground objects using the filtered three-dimensional ground penetrating radar data as represented by three types of images: A-, B-, and C-scans. In this study, we utilize a novel two-dimensional grid image consisting of several B- and C-scan images. Cavity, pipe, manhole, and intact features extracted from in situ three-dimensional ground penetrating radar data are used to train the convolutional neural network. The proposed technique is experimentally validated using real three-dimensional ground penetrating radar data obtained from urban roads in Seoul, South Korea.

Keywords

Ground penetrating radar, deep convolutional neural network, underground object detection, signal processing, basis pursuit

Introduction

Sinkholes are one of the most severe concerns for today's urban roads, because sudden ground collapses may lead not only to road closures and economic losses but also to human injuries and fatalities. Recently, several major sinkhole accidents have been reported worldwide, such as in Hangzhou, China (April 2016);¹ Fukuoka, Japan (November 2016);² and Cheltenham Township, PA, USA (January 2017).³ Extraction of groundwater, changes in water drainage patterns, and water main breakages are considered as the main causes of the underground cavities that lead to urban sinkholes.^{4,5} As sinkholes appear without any forewarning, there is an increasing demand for their early detection in urban areas. Several techniques have been developed to accomplish this. A commonly used geophysical inspection technique is electrical resistivity tomography (ERT). ERT has been widely used to

image subsurface structures by measuring the electrical resistivity.^{6,7} Although it is simple to implement and reliable for various applications such as investigations of the soil moisture content and the groundwater table, underground soil layers.

Alternatively, ground penetrating radar (GPR) has been widely used as a fully noncontact nondestructive testing technique. GPR is currently gaining popularity in the field of structural health monitoring thanks to its noncontact nature, fast scanning speed, and three-

¹Department of Architectural Engineering, Sejong University, Seoul, South Korea

²Department of Civil and Environmental Engineering, Sejong University, Seoul, South Korea

Corresponding author:

Yun-Kyu An, Department of Architectural Engineering, Sejong University, Seoul 05006, South Korea.

Email: yunkyu@sejong.ac.kr

dimensional (3D) imaging capability.⁸ **GPR** emits high-frequency electromagnetic waves into the ground and receives the returned electromagnetic waves reflected from underground objects. If there is any change in the electromagnetic characteristics, such as the relative permittivity of the medium or the subsurface composition, the boundaries of these anomalies can be identified through the received signal analysis. GPR has been primarily applied in archeological and geological contexts, where it is used for mapping subsurface features,^{9,10} and its use has been recently extended to the detection of underground cavities and potential sinkholes.^{11–13} However, raw GPR signals are typically difficult to be analyzed because of the governing role of reflections from the upper layer, such as the pavement. Moreover, data interpretation is made more challenging by the demanding conditions associated with urban roads, such as a complex geometry, variations in moisture content, and unexpected contaminants. The physical interpretation of the complex GPR data obtained from urban roads highly depends on experts' experience. However, expert-dependent data interpretation is time-consuming and labor-intensive. For example, an expert can analyze 3D GPR data of complex urban roads for only a few kilometers in a week, and these interpretation results may not be reliable.

In order to overcome these technical challenges, many researchers have been tried to enhance the visibility of structures in the original GPR image through representative GPR signal processing via subtraction¹⁴ or background removal methods.¹⁵ **However, the conventional GPR visualization filtering such as subtraction method, which eliminates the dominant surface reflections by subtracting a reference signal from the raw GPR data, is highly susceptible to noise and small signal disturbances in the time domain.** Sometimes, the GPR signals vary due to pavement thickness change or unexpected arbitrary boundary conditions of the pavement.¹⁶ In terms of automated underground object detection, a number of researchers have tried to use various signal processing tools such as curvelet transform,¹⁷ wavelet transforms^{18,19} and support vector machine.²⁰ Moreover, neural network classifiers were popularly utilized to classify underground objects. Al-Nuaimy et al. developed a neural network classifier to detect buried utilities and solid objects with GPR images,²¹ and Gamba et al. also used the neural network for detecting the pipe signatures in GPR image.²² Zhang et al. tried to use a machine learning technique by extracting the amplitude and time delay features from GPR B-scan images.²³ Although the conventional machine learning techniques were successfully used to detect dominant or clear features on GPR signals, they may not be suitable for underground multi-object classification, especially in complex urban areas. The

manual feature extraction and training processes are quite difficult and cumbersome tasks in complex *in situ* GPR data including a number of undesired similar features as well as measurement noises.

Recently, a deep convolutional neural network (CNN) has emerged to solve the complex data classification problem thanks to its advantages of self feature extraction, pre-training using unsupervised learning, the use of images themselves for the training and testing processes without image reconstruction and so on. By taking these advantages, the deep CNN incorporating with a noise filtering technique is employed for automated underground cavity detection in this study. Then, the proposed technique is experimentally validated using real 3D GPR data obtained from urban roads of Seoul city, South Korea. To authors' best knowledge, such experimental validation using in-situ 3D GPR data was rarely reported. First, a basis pursuit-based background filtering algorithm is developed, which is capable of automatically enhancing the visibility of underground objects beneath urban road pavements. The tailored CNN is then established by transfer learning using the well-pre-trained model of AlexNet.²⁴ Subsequently, the filtered 3D GPR data collected from *in situ* urban roads are used for training and validating the tailored CNN. The trained CNN is tested using various *in situ* 3D GPR data obtained from different urban roads.

This paper is organized as follows. Section 2 proposes the deep learning-based underground cavity detection technique. The performance of the proposed technique is experimentally validated using *in situ* 3D GPR data obtained from urban roads in Section 3. The paper is then briefly summarized, and the potential for extending it is discussed in Section 4.

Deep-learning-based automated underground cavity detection technique

The proposed deep learning-based technique for automated underground cavity detection is detailed below in the three steps. First, the data acquisition procedure and the various data formats obtained are described through a brief explanation of the working principles of multichannel GPR. The details of a basis pursuit-based background filtering algorithm that enhances the visibility of subsurface structures in the GPR images are then given. Finally, a tailored CNN designed to automatically detect underground cavities using the filtered images is described.

Working principles of **multichannel GPR**

Figure 1 schematically illustrates a typical GPR-based underground visualization process. 3D GPR consists of

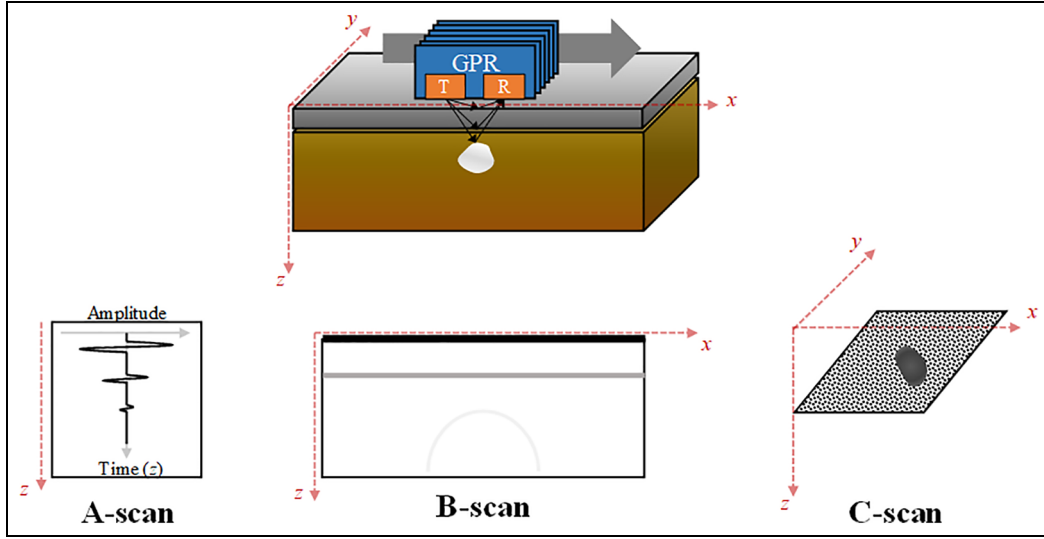


Figure 1. Working principles of GPR: T and R represent the transmitter and receiver antennas, respectively.

multiple transmitter and receiver antennas and a data acquisition system. The transmitter emits high-frequency electromagnetic waves, and the receiver receives the returned electromagnetic waves. The typical frequency range of the electromagnetic waves is several MHz to GHz; an appropriate range is selected depending on the size and depth of the target object. Essentially, high frequencies are used for shallower and smaller targets, and low frequencies are used for deeper and larger targets. If there is any change in the electromagnetic characteristics in the region scanned, such as a change in the relative permittivity of the ground layer or the presence of an anomalous object with different electromagnetic characteristics than the surrounding media, part of the electromagnetic wave is reflected back to the receiver antenna.²⁵ These reflected electromagnetic waves are then collected by the data acquisition system and subsequently analyzed for underground object detection. When the 3D GPR scans a region of interest, three different data types, A-, B-, and C-scans, are typically obtained, as shown in Figure 1. The A-scan provides punctual time-domain information (the z -axis in Figure 1) at a certain spatial point. The B-scan, in the x - z domain, is constructed on the basis of data from multiple A-scans along the scanning route (the x -axis in Figure 1). If there is an abrupt change in permittivity due to an underground object in a specific area, as shown in Figure 1, a parabolic feature will typically appear due to different propagations of the electromagnetic waves reflected from the underground object at each scanning spatial point. This parabola is often used to detect an underground object. The C-scan image can then be obtained in the x - y domain by combining B-scan images obtained using multiple antennas. Several

C-scan images can be obtained along the z -axis, which represents the depth. C-scan cross-sectional images of the object can then be used to characterize the detected feature further. Note that a dominant, nearly straight, linear feature often appears in the B-scan image due to a strong ground surface reflection. The ground surface reflection typically overwhelms the underground reflections because of the sudden permittivity change from the air (1 F/m^{-1}) to the pavement (5 F/m^{-1}). This linear feature in the B-scan images often impedes the detection of underground objects.

Basis pursuit-based background filtering algorithm

In this study, we developed a basis pursuit-based background filtering algorithm that is capable of improving the visibility of underground objects by removing the dominant linear feature in the B-scan images as well as unwanted pattern noises. The filtered image can significantly enhance underground object visibility, making it possible to use it effectively in the subsequent deep CNN process. Figure 2 provides an overview of the background filtering algorithm.

Step 1: collection of 3D GPR data and preprocessing. 3D GPR data are collected from each spatial scanning location along the region of interest, as illustrated in Figure 1. The measured GPR signals are typically attenuated when they propagate through a certain medium.²⁶ Thus, the preprocessing for wave attenuation in the depth direction is performed by applying gain factors to each A-scan.

Step 2: construction of a self-referencing dictionary. In order to enhance the identification of the interactions

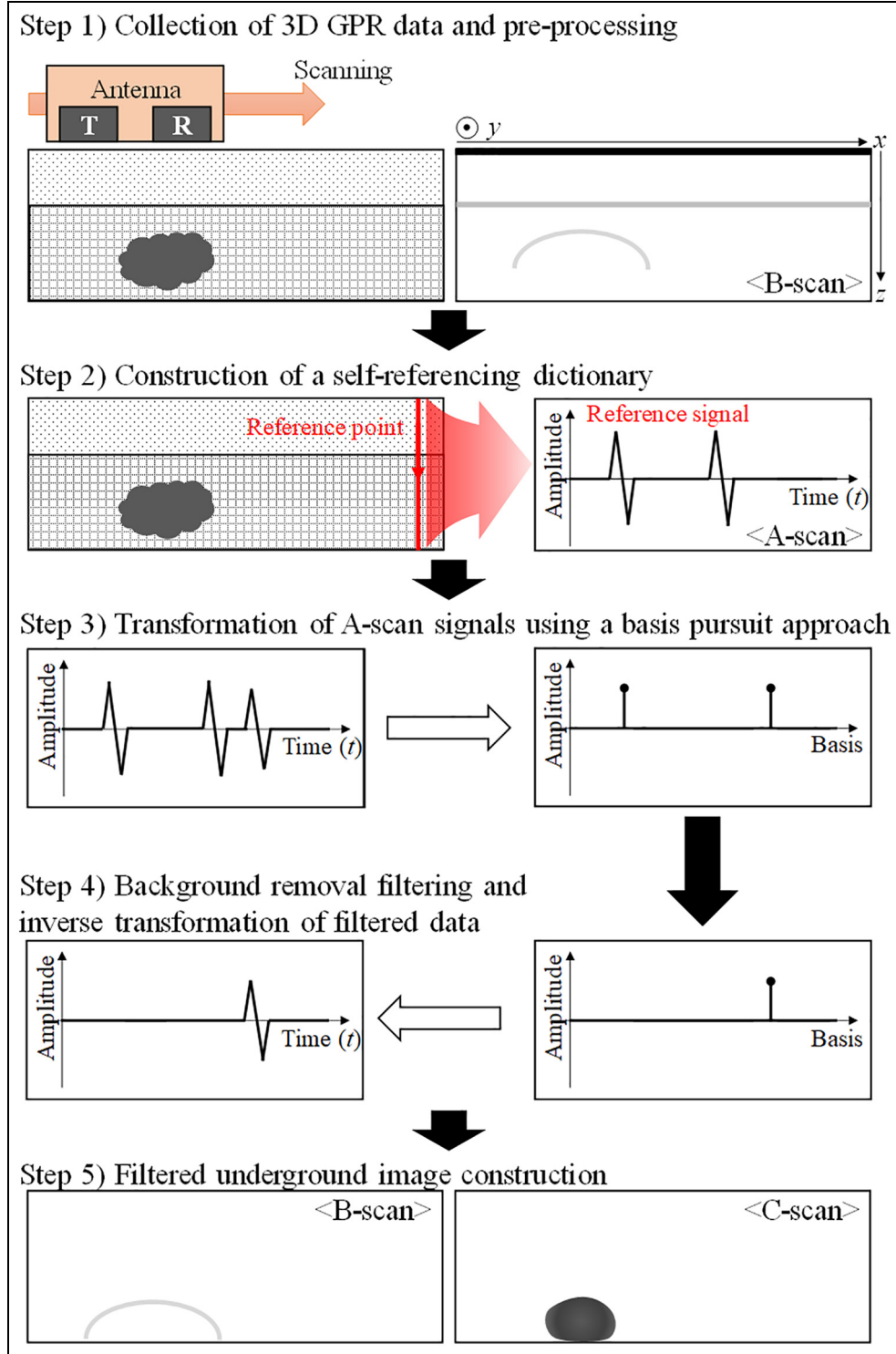


Figure 2. Schematic flow of the basis pursuit-based background filtering algorithm.

between the electromagnetic waves and underground objects, the measured A-scan signal, s ($T \times 1$ vector, where T is the length of the measured A-scan signal), is represented as a weighted linear combination of bases via the following transformation²⁷

$$s = D\alpha, \text{ where } D = \{d_1, d_2, \dots, d_L\} \quad (1)$$

where α is the representation of s in the transformed domain and has a dimension of $L \times 1$. D is the $T \times L$ dictionary matrix and consists of d_i bases ($i = 1, \dots, L$).

Each basis d_i is the A-scan signal with the same dimension as s .

Let us assume that we have a pristine scanning location without underground objects within the inspection area. This location is called a reference point, and the corresponding A-scan signal is called a reference signal

$$s = E_{\text{ref}}(t) = Ee^{-j\omega t} \quad (2)$$

where E_{ref} denotes the reference signal, E represents the amplitude of the incident electric field with a specific time delay, and ω refers to the frequency. Any change in s from the reference signal E_{ref} , such as underground object reflections, is compensated by adding weighted d_i with proper time delay. This is the time domain function represented by sum of multiple sinusoidal signals with different amplitudes and frequencies in Fourier transform. For example, d_i denotes the reference signal with a time delay of $(L/2 - i)\Delta t$. Since i is in the range of 1 to L , the bases are expressed $L/2$ to indicate the delay in the positive and negative directions

$$\begin{aligned} d_i &= E_{\text{ref}}(t + (L/2 - i)\Delta t) = E_{\text{ref}}(t + (L' - i)\Delta t) \\ &= E_{\text{ref}}e^{-j\omega(t + (L' - i)\Delta t)} \end{aligned} \quad (3)$$

Step 3: transformation of A-scan signals using a basis pursuit approach. Due to the fact that a large L value is preferred to achieve a high resolution in the transformed domain, typically an underdetermined system of equations ($L > T$) is used, creating non-unique solutions for α . A unique solution for α can be obtained via the assumption that the actual solution has the sparsest representation, minimizing the number of non-zero entities in α .²⁸ Based on this assumption, Chen and Donoho²⁹ proposed the basis pursuit approach to solve for an underdetermined system. The sparsest representation is obtained by solving the following problem with a given dictionary, D

$$\min \|\alpha\|_1 \quad s.t. s = D\alpha \quad (4)$$

where $\|\alpha\|_1$ denotes the ℓ_1 -norm of α . A-scan signals can be sparsely represented using the dictionary.

If the current scanning location does not include an underground object, the measured GPR signal, s , can be represented with only a single basis corresponding to the reference signal. This is the only nonzero element in α , and a sparse representation of the A-scan signal is possible in the dictionary domain. Then, s can be represented as

$$s = E_{\text{ref}}(t) = d_{L'} = d_{L'}\alpha_{L'} \quad (5)$$

where $d_{L'}$ and $\alpha_{L'}$ denote the basis and transformed domains of the reference signal, respectively. On the

other hand, equation (6) represents a GPR signal measured from a scanning location where there is an underground object in the dictionary domain. The measured signal, s , can be represented as the superposition of the reference signal and the reflected signal from the underground object

$$\begin{aligned} s &= E_{\text{ref}}(t) + E_{\text{ref}}(t + m\Delta t) = d_{L'}\alpha_{L'} + d_{L'-m}\alpha_{L'-m}, \\ &\text{where } m = L' - i \end{aligned} \quad (6)$$

where m represents the magnitude of the delay of the reflected signal in the sense of $L' - i$, and $m\Delta t$ indicates the depth of the underground object.

Step 4: background removal filtering and inverse transformation of filtered data. As described in equations (5) and (6), a new basis appears, as an underground object exists. The background signals can then be filtered out by removing the basis corresponding to the reference signal, $d_{L'}$. The resultant dictionary domain data are inversely transformed into A-scan signal data.

Step 5: filtered underground image construction. Finally, the underground image is constructed from the filtered A-scan data obtained in Step 4, making it possible to eliminate unnecessary background signals and highlight the reflected signals from the underground object.

Deep CNN-based automated underground cavity detection

A deep CNN architecture is then established, which can be applied to real 3D GPR data. Once the original image has been filtered through the basis pursuit-based technique, underground object images are automatically extracted through a deep CNN process. The B- and C-scan images were used in combination for the training and validation data sets, as shown in Figure 3. Many features visible in these images are helpful for enhancing the performance of the automated classification. Where there are reflections from underground objects, the B-scan images show parabolic features, as shown in Figure 3(a)–(c), in contrast to the intact case. However, a B-scan of a manhole (Figure 3(c)) has a distinct pattern of change with a dominant horizontal line between a double parabola due to the wave from the manhole being reflected from the uppermost surface. This distinct pattern makes it possible to distinguish the manhole case from the other cases easily. C-scan images in the depth direction for the cavity and pipe cases also show distinctive features. The C-scan of a cavity has a circular shape along the depth direction, whereas that in the pipe case has a rectangular shape. Where the subsurface is intact, no obvious pattern can be observed, as shown in Figure 3(d).

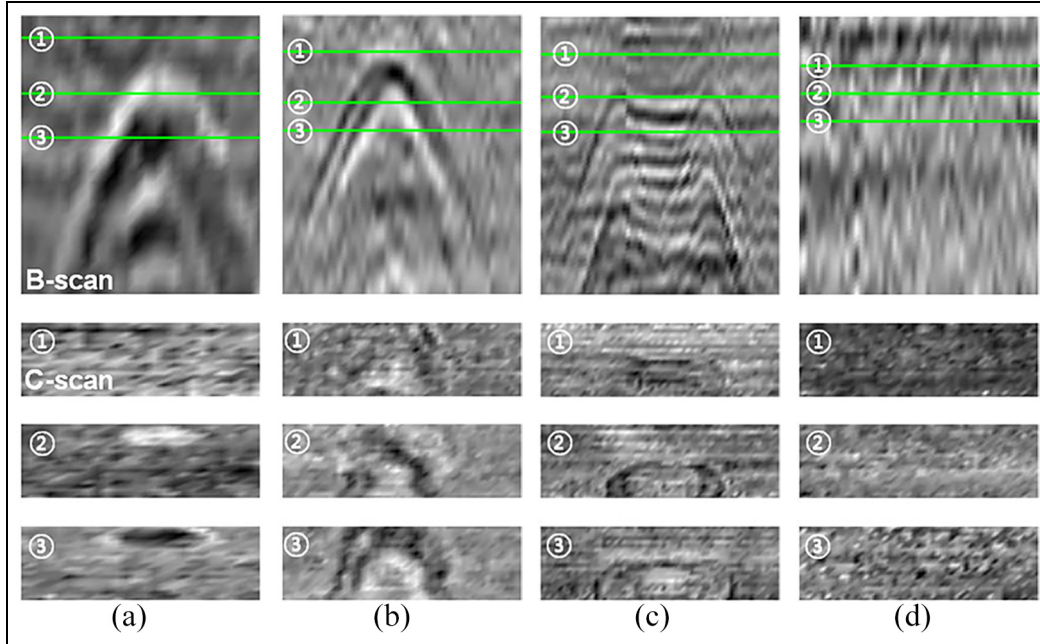


Figure 3. Typical B- and C-scan images: (a) cavity, (b) pipe, (c) manhole, and (d) intact.

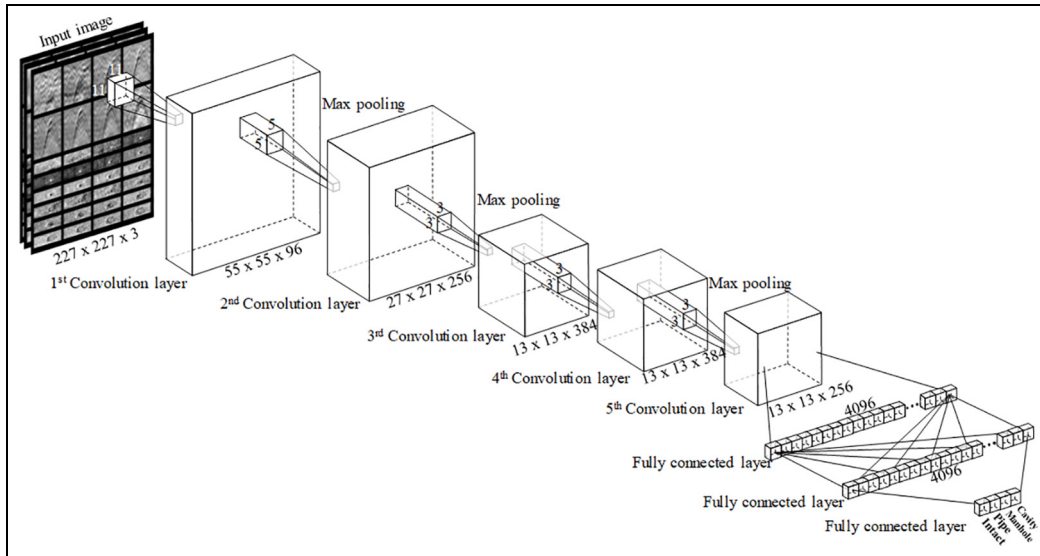


Figure 4. Deep CNN architecture tailored for 3D GPR data classification.

In this study, a pre-trained deep CNN model (i.e. AlexNet²⁴) was used for transfer learning. AlexNet is a well-known multilayered CNN model designed for visual pattern classification. It consists of five convolutional layers, three fully connected layers, and 1000 soft-max neurons, containing 650,000 neurons and 60 million parameters. To apply the AlexNet model for cavity detection, the end of AlexNet (i.e. after the fully connected layers) was retrained on a training set with

four classification outputs, that is, cavity, pipe, manhole, and intact.

The filtered B- and C-scan images were simultaneously reconstructed into a two-dimensional (2D) grid image consisting of 24 C-scan images and 8 B-scan images, as depicted in Figure 4. Although total 84 original images were gathered from in situ urban roads, they may not be enough to establish and verify the CNN architecture. In order to resolve this problem,

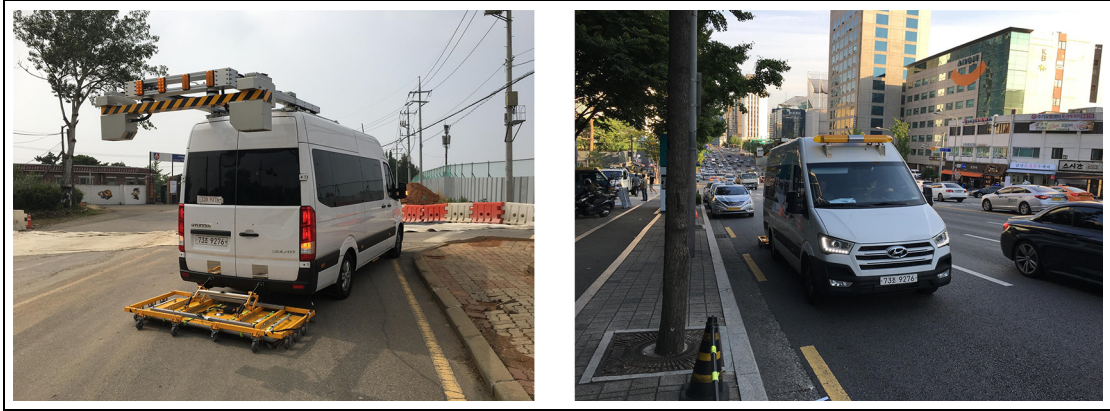


Figure 5. In situ tests using a van with a mounted 3D GPR.

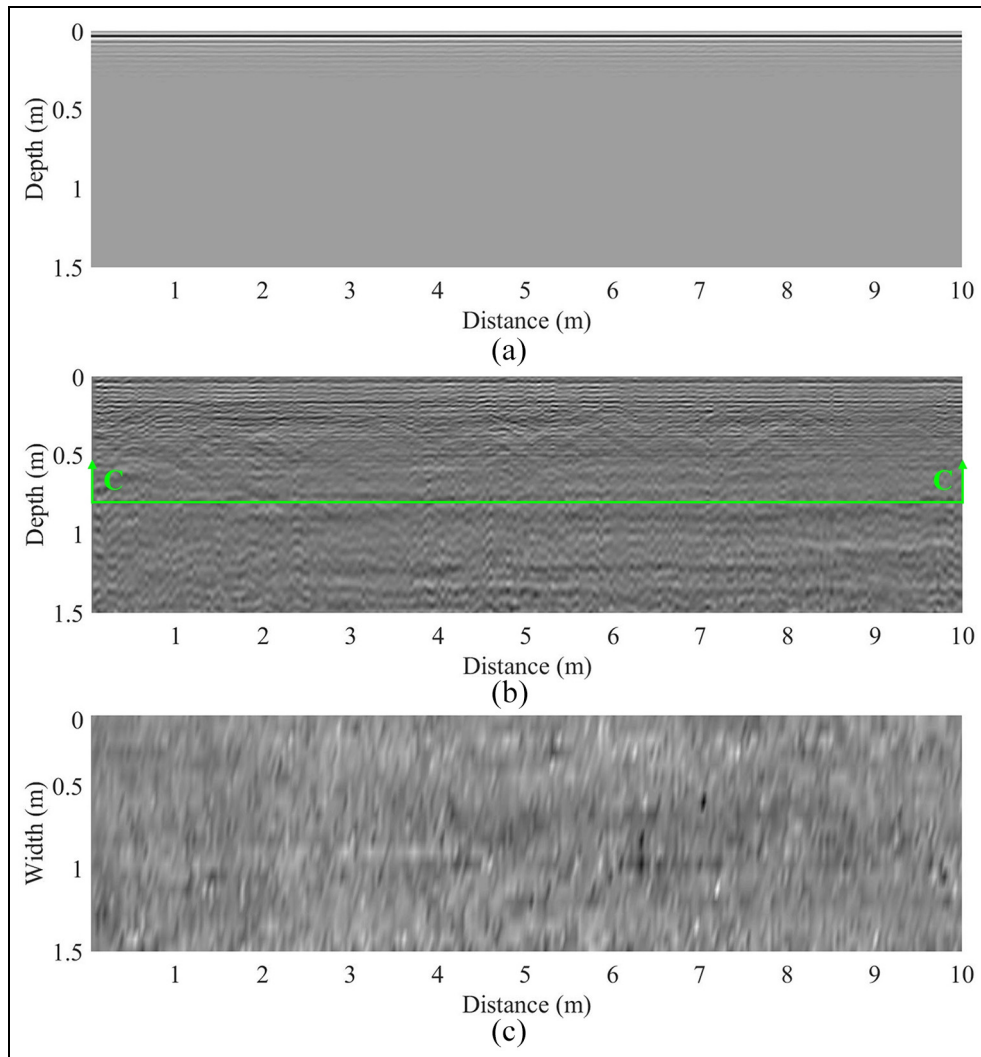


Figure 6. Representative results of basis pursuit-based background filtering for the intact case: (a) the original B-scan image obtained at 1.275 m from the left edge of the road, (b) the corresponding background filtered B-scan image, and (c) the corresponding filtered C-scan image at 0.7497 m depth, corresponding to the C-C line in (b).

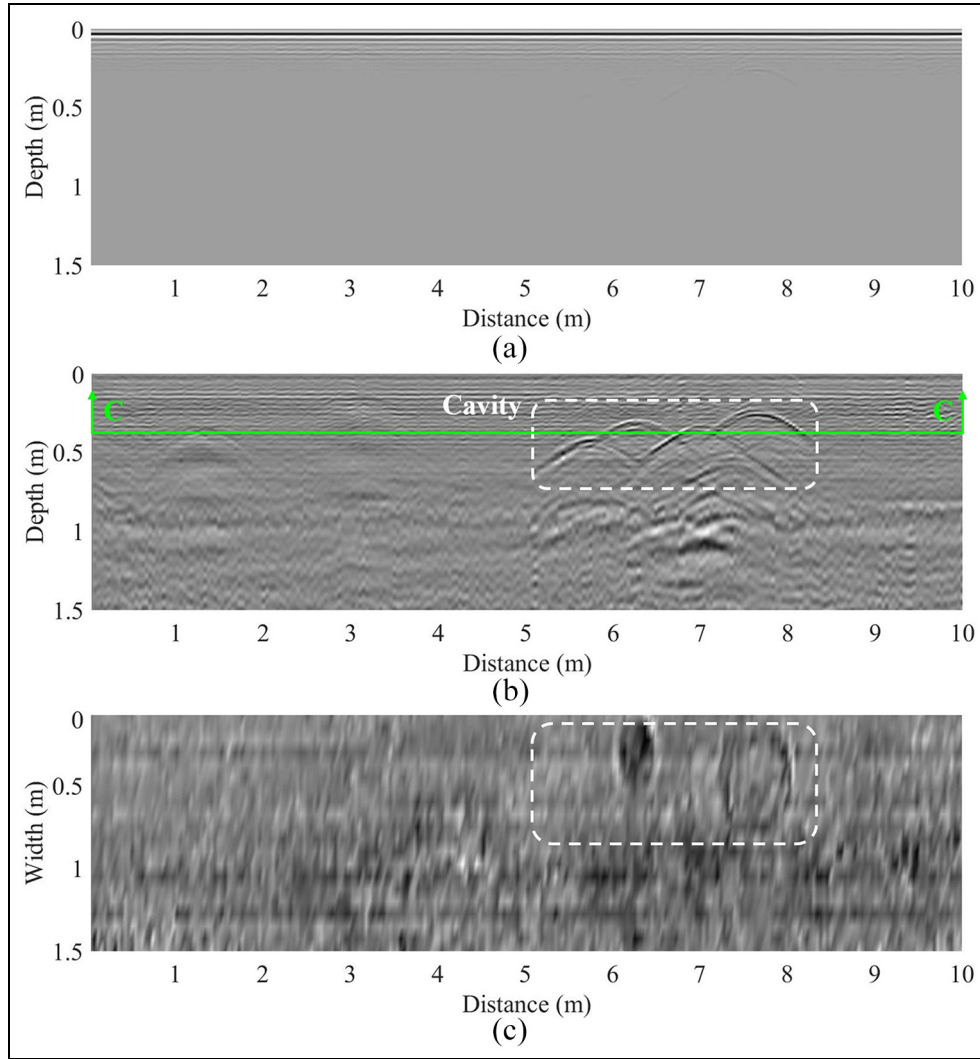


Figure 7. Representative results of basis pursuit-based background filtering for the cavity case: (a) the original B-scan image obtained at 0.375 m from the left edge of the road, (b) the corresponding background filtered B-scan image, and (c) the corresponding filtered C-scan image at 0.3517 m depth, corresponding to the C-C line in (b).

additional images were augmented by shifting an original underground image in upward, downward, left and right directions up to several pixels each. Among them, 4368 cavity, 4914 pipe, 3003 manhole, and 1638 intact images were used for network training, and another 819 cavity, 819 pipe, 546 manhole, and 273 intact images were randomly selected as the validation set. The remaining 2184 cavity, 2184 pipe, 1365 manhole, and 819 intact images were used for network testing. All the prepared images were 227×227 pixels, maintaining an aspect ratio appropriate for the AlexNet input layer, and the training and validation sets were distinct from each other. Note that NVIDIA Titan Xp, which is the high-performance graphic processing unit with memory of 12 gigabytes and 3840 cores, was employed to expedite the network training and classification processes.

Field validation tests

The proposed deep-learning-based automated underground cavity detection technique was experimentally validated using 3D GPR data collected from urban roads in Seoul, South Korea.

Experimental setup

Figure 5 shows the implementation of in situ data collection via the integration of a 3D GPR device with a vehicle. The vehicle can scan a 1.5 m width of road at speeds of up to 30 km/h. The used 3D GPR antenna is the DXG1820³⁰ manufactured by 3D-RADAR. This antenna includes 20 transmitter and receiver channels, specially designed for a 1.5 m scanning

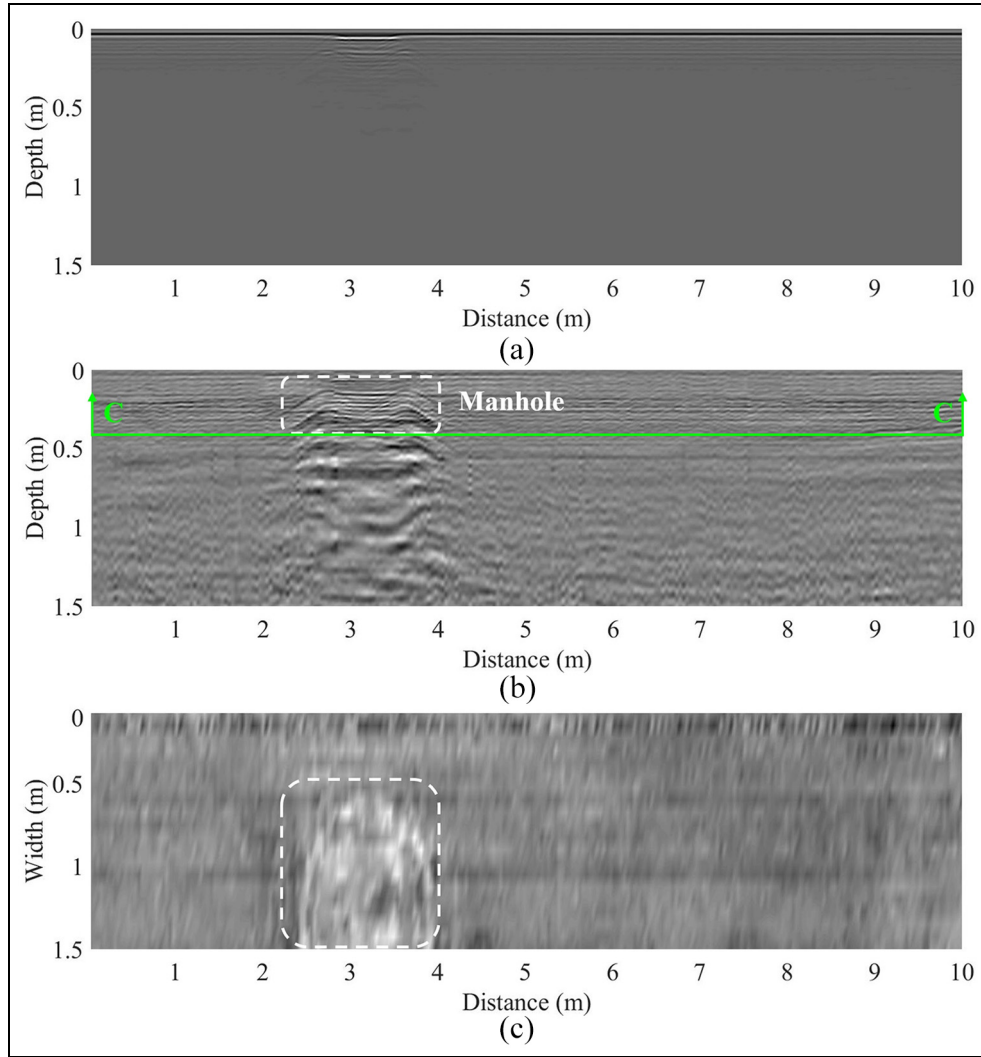


Figure 8. Representative results of basis pursuit-based background filtering for the manhole case: (a) the original B-scan image obtained at 1.125 m from the left edge of the road, (b) the corresponding background filtered B-scan image, and (c) the corresponding filtered C-scan image at 0.459 m depth, corresponding to the C-C line in (b).

width. The GPR signals are collected by the GEOSCOPE MK IV³⁰ data acquisition system in real time with a time resolution of 0.34 ns and a maximum scanning rate of 13,000 Hz. For the validation tests, a total of 13 km of urban roads in 17 different regions in Seoul, South Korea, were scanned. The existence of a cavity in the core was checked with a portable endoscope.

Results of basis pursuit-based background filtering

Intact case. The basis pursuit-based background filtering algorithm was first applied to the intact region containing no underground objects. Figure 6(a) shows the representative B-scan image at 1.275 m from the left edge of the C-scan (0 m width). No reflection from

underground objects is observed, but dominant surface pavement reflections are shown near the pavement surface. The background filtering technique was applied to this region to enhance any reflections from underground objects. Here, the leftmost scanning location in the region was selected as the reference point, and the corresponding response was considered as the reference signal. After filtering, there was still a lack of distinguishable features (Figure 6(b)), but minor parabolas were seen near the surface layer. Figure 6(c) shows the representative C-scan of the region at 0.7497 m depth after filtering, corresponding to the C-C line in Figure 6(b). No features are visible in this image. These results indicate that the proposed technique is valid for an intact region without giving false positives suggesting an underground object.

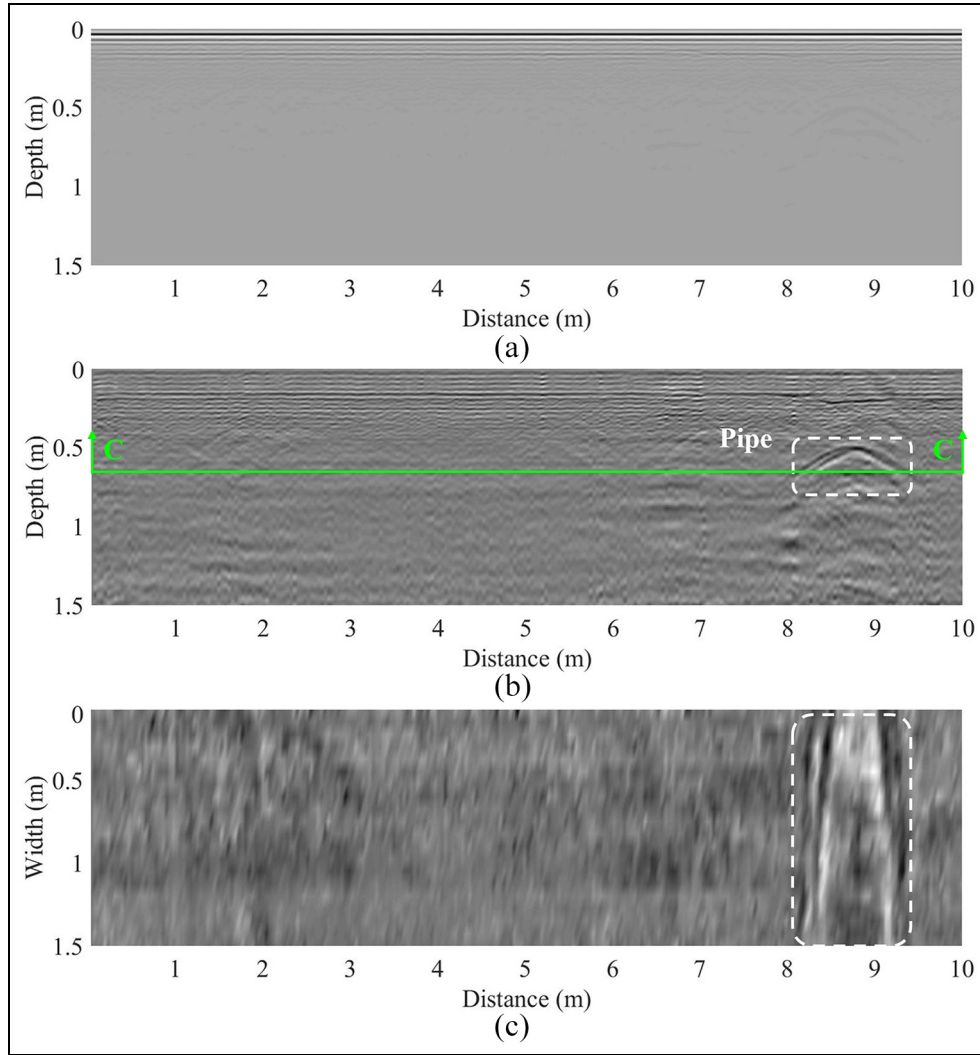


Figure 9. Representative results of basis pursuit-based background filtering for the pipe case: (a) the original B-scan image obtained at 1.2 m from the left edge of the road, (b) the corresponding background filtered B-scan image, and (c) the corresponding filtered C-scan image at 0.663 m depth, corresponding to the C-C line in (b).

Cavity case. Figure 7(a) shows a representative original B-scan image collected at 0.375 m from the left edge of the road. As expected, the near-surface linear feature caused by reflection from the pavement surface is again predominant, hindering the visualization of underground reflection features. After background filtering, underground parabolas in the B-scan image and circular cross-sectional features in the C-scan image are clearly observed in Figure 7(b) and (c), respectively.

Manhole case. Manholes are located in the uppermost pavement surface. In Figure 8(a), although the surface pavement reflections are dominant, the manhole can be seen in the original B-scan at 1.125 m from the edge of the road due to the large difference in the relative

permittivity between the surface pavement and the manhole. However, the manhole becomes more clearly visible after background filtering. Figure 8(b) and (c) shows, respectively, representative B- and C-scans of the region at 1.125 m width and 0.459 m depth.

Pipe case. Pipe reflection signals are more clearly visible after background filtering (Figure 9(b)) than in the original B-scan at 1.2 m width (Figure. 9(a)). Although these pipe reflection signals are often misclassified as indicative of a cavity on the basis of the B-scan, the C-scan at 0.663 m depth clearly shows them to have a rectangular shape, revealing an underground pipe buried perpendicular to the 3D GPR scanning direction (Figure 9(c)).

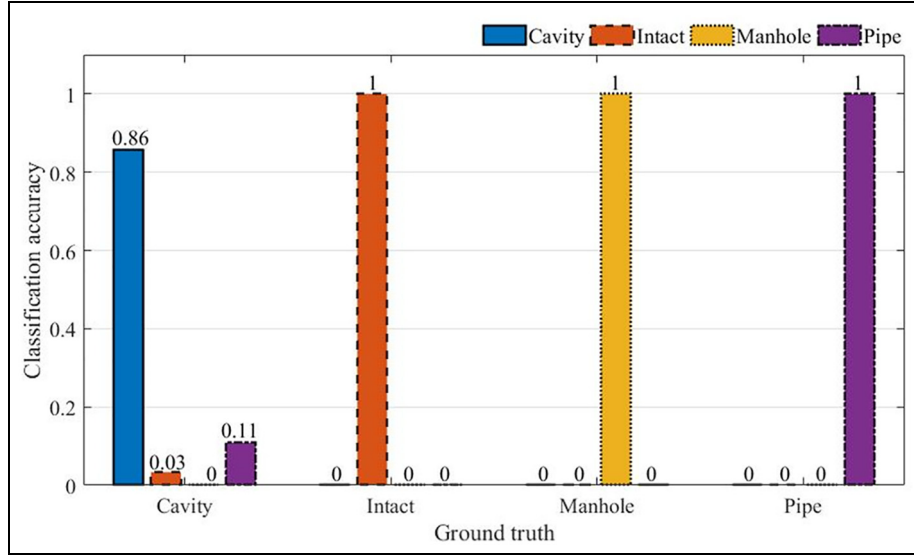


Figure 10. Results of underground object classification.

Table 1. The number of cavity, manhole, pipe, and intact data sets for training, validation, and testing.

Type	Number of training images	Number of validation images	Number of testing images
Cavity	4368	819	2184
Pipe	4914	819	2184
Manhole	3003	546	1365
Intact	1638	273	819

Table 2. Statistical results obtained from the deep CNN process.

Type	Precision (%)	Recall (%)	F-score (%)
Cavity	100	85.76	92.33
Pipe	90.17	100	94.83
Manhole	100	100	100
Intact	91.82	100	95.73

CNN: convolutional neural network.

Automated underground cavity detection using the deep CNN process

Once the filtered B- and C-scan images have been prepared for the validation tests, they were fed into the trained CNN. 13 km of GPR data, containing 27 cavities, 16 manholes, 26 pipes, and 9 intact cases, were used for training and testing, and its total training and testing time takes around 20 min or so. The number of images related to the GPR data for underground objects were increased through shifting of the original

images to reach the numbers summarized in Table 1. The overall results of the classification are shown in Figure 10. The x -axis and y -axis indicate the correct classification (i.e. ground truth) and the classification accuracy, respectively. All test cases were successfully classified using the trained CNN, except for the cavity case. Since the cavity and pipe cases are different in size and have different burial depths, 11% of the cavity test cases were misclassified as pipes, although the remaining 86% of the data sets were properly classified as cavities. In addition, dozens of weak reflected signals from small cavities were misclassified as intact.

The performance of the automated underground cavity detection technique is evaluated by calculating statistical indices such as precision, recall, and F -score using equation (7).³¹ Table 2 summarizes the statistical results obtained from the deep CNN process. The precision values for pipes and an intact subsurface, indicating that the images physically represent a false positive, are relatively low because the deep CNN process sometimes recognizes a cavity as a pipe or intact. The recall value for cavities is also relatively low for the same reason. On the other hand, the precision and recall values for a manhole, corresponding to a false positive and false negative, are relatively high, meaning that manholes are properly classified by the deep CNN process. According to the F -scores, which physically combine both false positives and false negatives, it can be concluded that the performance of the proposed technique was acceptable. However, it is speculated that reinforced learning using more high-quality data sets and additional classification procedures may help enhance them.

$$\begin{aligned}
 \text{Precision} &= \frac{\text{true positive}}{\text{true positive} + \text{false positive}} \\
 \text{Recall} &= \frac{\text{true positive}}{\text{true positive} + \text{false negative}} \\
 F - \text{score} &= \frac{2 \times (\text{Precision} \times \text{Recall})}{\text{Precision} + \text{Recall}}
 \end{aligned} \quad (7)$$

Conclusion

In this article, we proposed a deep-learning-based automated technique for underground cavity detection. This technique outperforms existing GPR techniques in which fast and fully automated data interpretation can be achieved. The proposed technique was experimentally validated using real 3D GPR data for urban roads in Seoul, South Korea. Such data are rarely available and present a unique opportunity for testing the methodology. Although the proposed technique showed an acceptable accuracy in detecting underground cavities, technical improvements using a reinforced learning process are desirable. However, the GPR signals reflected from underground rocks or gravel having similar shape with cavity are not often indistinguishable from the underground cavity ones. It might be difficult to identify the cavity using only filtered B- and C-scan images. To overcome the technical limitation, more high-quality training data sets confirmed by drilling of boreholes are now being gathered and used for reinforced learning and constructing robust GPR data library. Furthermore, additional signal processing techniques such as the phase analysis of A-scan signals will be developed and combined with current deep CNN architecture as the following study, making it possible to enhance the automated classification accuracy of various types of underground objects.



Declaration of conflicting interests

The author(s) declared no potential conflicts of interest with respect to the research, authorship, and/or publication of this article.

Funding

The author(s) disclosed receipt of the following financial support for the research, authorship, and/or publication of this article: This research was supported by the grant 18TLRP-C099510-04 from the Construction Technology Research Program, which is funded by the Ministry of Land, Infrastructure, and Transport of the Korean Government.

ORCID iDs

Jong Jae Lee  <https://orcid.org/0000-0003-0672-5160>
 Yun-Kyu An  <https://orcid.org/0000-0003-2916-4917>

References

1. Sims A. Huge sinkhole opens at busy Chinese intersection, <http://www.independent.co.uk/news/world/asia/huge-sinkhole-opens-at-busy-chinese-intersection-a7000321.html> (2016, accessed 19 July 2018).
2. BBC News. Huge sinkhole swallows street in Fukuoka, Japan. <http://www.bbc.com/news/world-asia-37906065> (2016, accessed 19 July 2017).
3. Jimenez T. Massive sinkhole nearly swallows home in Pennsylvania. <http://philadelphia.cbslocal.com/2017/01/25/massive-sinkhole-opens-up-in-cheltenham-twp/> (2017, accessed 19 July 2017).
4. Gutierrez F, Parise M, Waele J, et al. A review on natural and human-induced geohazards and impacts in karst. *Earth Sci Rev* 2014; 138: 61–88.
5. Perlow M. An overview of recent sinkhole problems in the Lehigh valley, Pennsylvania. In: *Proceedings of the 9th multidisciplinary conference on sinkholes and the engineering and environmental impacts of karst*, Huntsville, AL, 6–10 September 2003.
6. Griffiths D and Barker R. Two-dimensional resistivity imaging and modelling in areas of complex geology. *J Appl Geophys* 1993; 29: 211–226.
7. Schoor M. Detection of sinkholes using 2D electrical resistivity imaging. *J Appl Geophys* 2002; 50: 393–399.
8. Chang P, Flatau A and Liu S. Review paper: health monitoring of civil infrastructure. *Struct Health Monit* 2003; 2: 257–267.
9. Nuzzo L, Leucci G, Negri S, et al. Application of 3D visualization techniques in the analysis of GPR data for archaeology. *Ann Geophys Italy* 2002; 45: 321–337.
10. Conyers L. *Ground-penetrating radar for archaeology*. 3rd ed. Plymouth: Routledge, 2013.
11. Batayneh A, Abdelruhman A and Moumani K. Use of ground-penetrating radar for assessment of potential sinkhole conditions: an example from Ghor al Haditha area, Jordan. *Environ Geol* 2002; 41: 977–983.
12. Pueyo-Anchuela O, Juan A, Soriano M, et al. Characterization of karst hazards from the perspective of the doline triangle using GPR—examples from Central Ebro Basin (Spain). *Eng Geol* 2009; 108: 225–236.
13. Rodriguez V, Gutiérrez F, Green A, et al. Characterizing sagging and collapse sinkholes in a Mantled Karst by means of ground penetrating radar (GPR). *Environ Eng Geoscience* 2014; 20: 109–132.
14. Benedetto A, Tosti F, Ciampoli L, et al. An overview of ground-penetrating radar signal processing techniques for road inspections. *Signal Process* 2017; 132: 201–209.
15. Annan A. *Practical processing of GPR data*. Mississauga, ON, Canada: Sensors & Software, 1999.
16. Park B, Kim J, Lee J, et al. Underground object classification for urban roads using instantaneous phase analysis of ground-penetrating radar (GPR) data. *Remote Sens* 2018; 10: 1417.
17. Tzanis A. The curvelet transform in the analysis of 2-D GPR data: signal enhancement and extraction of orientation-and-scale-dependent information. *J Appl Geophys* 2015; 115: 145–170.

18. Tzanis A. Detection and extraction of orientation-and-scale-dependent information from two-dimensional GPR data with tuneable directional wavelet filters. *J Appl Geophys* 2013; 89: 48–67.
19. Bailia J, Lahouara S, Herglia M, et al. GPR signal denoising by discrete wavelet transform. *NDT&E Int* 2009; 42: 696–703.
20. Qin Y and Huang C. Identifying underground voids using a GPR circular-end bow-tie antenna system based on a support vector machine. *Int J Remote Sens* 2016; 37: 876–888.
21. Al-Nuaimy W, Huang Y, Nakhkash M, et al. Automatic detection of buried utilities and solid objects with GPR using neural networks and pattern recognition. *J Appl Geophys* 2000; 43: 157–165.
22. Gamba P. Neural detection of pipe signatures in ground penetrating radar images. *IEEE Trans Geosci Remote Sens* 2000; 38: 790–797.
23. Zhang Y, Huston D and Xia T. Underground object characterization based on neural networks for ground penetrating radar data. In: *Proceedings of the SPIE*, Nevada, US, 8 April 2016, pp.1–9.
24. Krizhevsky A, Sutskever I and Hilton G. ImageNet classification with deep convolutional neural networks. In: *Advances in Neural Information Processing Systems*, Nevada, US, 3–6 December 2012, pp. 1097–1105.
25. Griffiths D. *Introduction to electrodynamics*. 4th ed. London, UK, 2012.
26. Jol H. *Ground penetrating radar theory and applications*. Amsterdam, Netherlands, 2009.
27. Anton H and Busby R. *Contemporary linear algebra*. New York, US, 2003.
28. Gribonval R and Nielsen M. Sparse representations in unions of bases. *IEEE Trans Inform Theory* 2003; 49: 3320–3325.
29. Chen S and Donoho D. Basis pursuit. In: *Proceedings of 28th Asilomar Conference on Signals, Systems and Computers*, California, United States, 31 October–2 November 1994.
30. 3d-radar company. <http://3d-radar.com/> (2001, accessed 19 July 2018).
31. Sasaki Y. *The truth of the F-measure*. Manchester, UK: University of Manchester, 2007.